JOURNAL OF GEOPHYSICAL RESEARCH, VOL. 100, NO. B10, PAGES 20,433–20,450, OCTOBER 10, 1995

Channeling instability of upwelling melt in the mantle

E. Aharonov
Department of Earth, Atmospheric and Planetary Sciences, Massachusetts Institute of Technology, Cambridge, Massachusetts

J. A. Whitehead and P. B. Kelemen
Woods Hole Oceanographic Institution, Woods Hole, Massachusetts

M. Spiegelman
Lamont-Doherty Earth Observatory of Columbia University, Palisades, New York

Abstract. We present results of a theoretical study aimed at understanding melt extraction from the upper mantle. Specifically, we address mechanisms for focusing of porous flow of melt into conduits beneath mid-ocean ridges in order to explain the observation that most oceanic residual peridotites are not in equilibrium with mid-ocean ridge basalt. The existence of such conduits might also explain geological features, termed replacive dunites, that are observed in exposed mantle sections. We show here, by linear analysis, that flow in a chemically reactive porous media is unstable in the presence of a solubility gradient, such as induced by adiabatic ascent of melt underneath mid-ocean ridges. The initially homogeneous flow becomes focused in time to produce elongated high-porosity fingers that act as conduits for transport of fast flowing melt. This instability arises due to a positive feedback mechanism in which a region of slightly higher than average porosity causes increased influx of unsaturated flow, leading to increased dissolution which further reduces the porosity. Even in the presence of matrix compaction and chemical diffusion the instability is demonstrated to be robust. Our analysis also indicates the existence of growing, traveling waves which transport and amplify porosity and concentration perturbations.

Introduction

Recent work [*Klein and Langmuir*, 1987; *Salters and Hart*, 1989; *Johnson et al.*, 1990; *Johnson and Dick*, 1992] indicates that upwelling mid-ocean ridges basalt (MORB) is in chemical disequilibrium with the upper mantle peridotites that constitute the matrix through which it flows. These observations place constraints on melting and melt extraction processes at ridges. In order to produce disequilibrium transport, small melt fractions must be efficiently segregated from their source and transported to the crust [*Johnson et al.*, 1990; *Johnson and Dick*, 1992; *Sobolev and Shimizu*, 1993; *Iwamori*, 1993]. Since diffuse porous flow of melt along grain boundaries would lead to extensive chemical reaction and erasure of observed trace element fractionation, some form of focused flow of melt into channels has been proposed to explain extraction of MORB from the mantle [*Spiegelman and Kenyon*, 1992; *Hart*, 1993].

The results of our study imply that one of the mechanisms responsible for focusing may be a coupled chemical-hydrodynamical instability; uniform upwelling of melt flowing through a porous media is unstable when the melt is dissolving some of the matrix through which it is flowing and begins to form elongated, high-porosity channels. In ophiolites, geological observation of dissolution channels (dunites) in chemical equilibrium with MORB, surrounded by mantle peridotites which are not in chemical equilibrium with MORB, confirms that this instability may operate during melt extraction from the mantle at oceanic spreading ridges [*Kelemen*, 1990; *Kelemen et al.*, 1994, 1995a].

Additional mechanisms for melt extraction from the mantle beneath mid-ocean ridges could include (1) hydrofracture [e.g., *Nicolas*, 1990]; (2) focused flow of melt in zones of localized, active deformation [e.g., *Stevenson*, 1989; *Kelemen and Dick*, 1995]; and (3) decompaction into melt-filled lenses or veins [*Sleep*, 1988, also production of veins by magma solitons, submitted to *J. Geophys. Res.*, 1994]. Mechanisms 1 and 2 are most probable near and above the brittle/ductile transition in the mantle, where strain becomes localized into shear zones. This is supported by geological evidence that dikes and localized shear zones in the mantle section of ophiolites form mostly "off-axis," away from a spreading ridge, near the brittle-ductile transition, and not in the adiabatically ascending, partially melting man-

Paper number 95JB1307.
0148-0227/95/95JB-01307$05.00

tle beneath a spreading ridge [*Kelemen and Dick*, 1995; *Kelemen et al.*, 1995b]. The third possible mechanism is poorly understood at present, and we are not aware of geological evidence supporting such a hypothesis. In contrast, the reactive infiltration instability is likely to operate in adiabatically upwelling, partially molten, ductile asthenosphere, and there is geologic evidence for focused flow of melt in porous dissolution channels in the mantle section of ophiolites.

It has been known for some time [*Chadam et al.*, 1986; *Ortoleva et al.*, 1987; *Hinch and Bhatt*, 1990] that reactive flow through a soluble porous matrix may result in formation of finger-like embayments along an advancing reaction front. The mechanism for this instability, termed the "reactive infiltration instability" (RII), is simple: when unsaturated fluid flows through a soluble matrix, a region with slightly higher than average porosity will tend to have an increased influx of fluid, which will increase the rate of dissolution and so increase the porosity even further, in a positive feedback mechanism. Increased velocity in localized regions will cause lateral convergence of fluid upstream of the front into the high-porosity fingers [*Kelemen et al.*, 1995a].

The characteristic wavelengths and growth rates of the front instability are determined by three parameters: chemical reaction rate, transport rate, and diffusion rate [*Steefel and Lasaga*, 1990]. Reaction and diffusion act to restore the system to equilibrium, while advection acts to make it unstable. When diffusion is strong (compared with reaction), it will act as the main stabilizing mechanism for this instability. The most unstable wavelength in this case is determined by competition between advection (which drives the instability) and diffusion (which tends to smooth perturbations). The ratio between these parameters is termed Pe, the Peclet number.

Work on the RII with reaction-controlled smoothing is sparse but generally indicates that growing fingers are present [*Hoefner and Fogler*, 1988; *Steefel and Lasaga*, 1990]. Da, the Damköhler number, is the ratio between reaction timescale and advection timescale and is the control parameter in this case. Hoefner and Fogler performed experiments and network simulations which indicate a dependence of coalescing or branching of dissolution channels on Da.

Past work on this subject is not directly applicable to Earth's mantle. The front problem as reviewed above is transient; there is no supply of new grains to the system, and once the reaction front has propagated through the matrix there are no porosity perturbations left. Moreover, the instability (area of disequilibrium) is localized to a single interface between two areas of equilibrium rather than affecting the entire interior solution (although Hinch and Bhatt consider the case of a front of finite width). We see no evidence for the existence of such a propagating reaction front in the mantle, no evidence of a sharp reaction zone underneath which the mantle is composed purely of olivine and above which it is composed of pyroxene. In this paper, we investigate instabilities arising in a steady state mantle, where some background porosity, solid and liquid velocities, and mineral composition can be assumed. In this case there are no transient solution fronts, and if an instability arises, it will be present in the whole region of upwelling and dissolution.

In the mantle, decompression of ascending melt underneath mid-ocean ridges causes an increase in solubility of solid phases with height [*Sleep*, 1975; *Kelemen et al.*, 1995a]. Choosing a point along the ascent path of the melt, one can see that dissolution at this point increases the local concentration of soluble components in the melt but never to the point of equilibrium, since upward flow keeps bringing in undersaturated melt. This small departure from equilibrium allows an instability to occur, in the same manner as the feedback mechanism for the dissolution front described above. However, instead of having a fingered front, we expect the instability to occur within the region of melt transport wherever there exists a gradient in solubility.

In this paper we study a porous matrix confined in a box where grains are soluble, and there is a constant flux of melt from the lower end of the box. As solid material dissolves, the matrix is allowed to contract by compaction so as to keep the porosity constant in the steady state, with additional grains supplied at the top of the box. The solubility of the grains increases linearly with increasing height in order to approximate the increase in solubility induced by adiabatic ascent of melt decompressing in the mantle. Thermal melting of the solid phases, as distinguished from reactive dissolution, is neglected, as is viscous shearing of the solid phases and advective heat transport by melt. In what follows, we present the governing equations, nondimensionalize them, find a possible steady state, and do a linear stability analysis.

Two interesting unstable features are then shown to coexist:

1. The system is shown to be linearly unstable to small perturbations, causing focusing of flow in elongated high-porosity channels, where the vertical dimension is generally much longer than the horizontal dimension, establishing conduits for ascent of melt. These channels form provided that the characteristic length for chemical equilibration is smaller than a characteristic length for compaction. A calculation using characteristic values for Earth's mantle predicts that the condition for formation of the instability is probably met and that the reaction-infiltration instability may play an important role in forming conduits for melt extraction from the mantle.

2. The system gives rise to unstable propagating waves, which in the limit of no dissolution are linear compaction waves [*Spiegelman*, 1993a]. The addition of dissolution during porous flow gives rise to waves whose amplitude increases with time, providing dissolution features which propagate in space with a finite phase and group velocity. These results suggest a mechanism for spontaneous nucleation of "magmons" [*Scott and Stevenson*, 1986; *Spiegelman*, 1993c].

Finally, we discuss the application of our study to focusing of melt flow in the mantle beneath mid-ocean ridges.

Formulation of the Problem

General Equations

In this section we present a set of equations describing the essence of reactive flow through a soluble porous medium with a gradient in solubility. The setup of the problem is given in Figure 1. Fluid is driven upward by a pressure gradient, entering the soluble matrix at $z = 0$ and leaving it at $z = L$. With decreasing pressure the fluid has increasing ability to dissolve the porous matrix. Since we would like to investigate a steady state and deviations from it, we have allowed for compaction, though it is by no means crucial for the growth of the instability. Compaction provides a relatively simple steady state where dissolution increases the porosity and compaction works to decrease it.

The set of governing equations presented below closely follows the notation and form of some previous work on deformable porous media [*McKenzie*, 1984; *Scott and Stevenson*, 1986; *Spiegelman*, 1993a, 1993b]. This approach views the coupled solid-fluid system as two interpenetrating fluids with vastly different viscosities and is valid for length scales much larger than a pore size. Inertial effects have been assumed to be negligible.

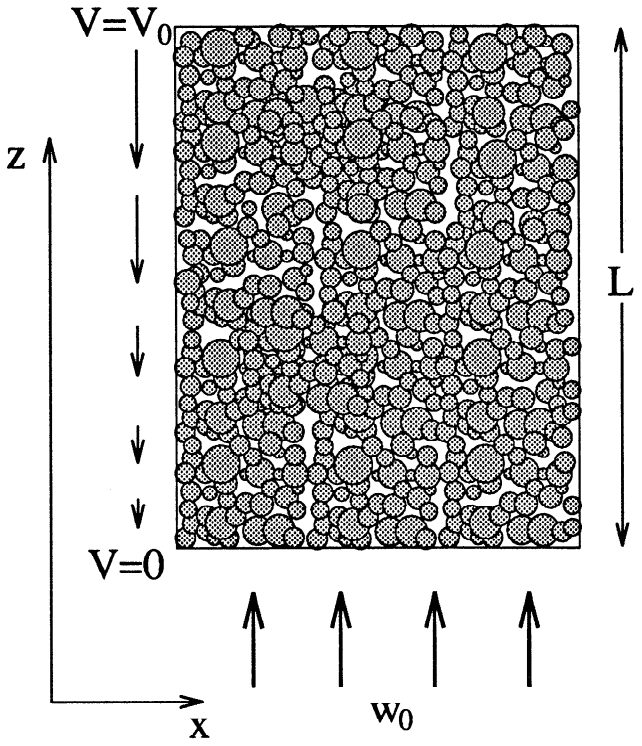

Figure 1. Setup of the problem: Fluid is driven upward by a pressure gradient, entering the soluble porous media at $z = 0$ and leaving at $z = L$. Owing to decompression, the fluid has increasing ability to dissolve the solid matrix. The matrix is allowed to contract by compaction and thus counteract to some degree the effects of increasing dissolution.

Conservation of mass. Conservation of the solid phase is given by

$$\frac{\partial \rho_s(1-\phi)}{\partial t} + \nabla \cdot [\rho_s \mathbf{V}(1-\phi)] = -\sum_i \Gamma_i, \quad (1)$$

where ϕ is the porosity, ρ_s is the solid density in kg m^{-3}, $\mathbf{V}$ is the solid grain velocity vector and Γ_i is the mass transfer rate of mineral i from solid to fluid in kg m^{-3} $s^{-}1$.

Conservation of fluid mass is given by

$$\frac{\partial \rho_f \phi}{\partial t} + \nabla \cdot (\rho_f \mathbf{v}\phi) = \sum_i \Gamma_i, \quad (2)$$

where ρ_f is the density of the fluid and $\mathbf{v}$ is the fluid velocity vector.

Component conservation equations in the fluid phase consist of three contributions: diffusion, advection, and a chemical source/sink term:

$$\frac{\partial \rho_f \phi c_i}{\partial t} + \nabla \cdot (\rho_f \phi \mathbf{v} c_i) = \nabla \cdot (D_i \rho_f \phi \nabla c_i) + \Gamma_i, \quad (3)$$

where D_i is the diffusion coefficient of component i in the fluid and c_i is the mass fraction of dissolved component i in the fluid, with $\sum_i c_i = 1$.

Each individual component is also conserved in the solid phase such that

$$\frac{\partial \rho_s(1-\phi)c_i^s}{\partial t} + \nabla \cdot [\rho_s(1-\phi)\mathbf{V}c_i^s] = \nabla \cdot [D_i^s \rho_s(1-\phi)\nabla c_i^s] - \Gamma_i, \quad (4)$$

where c_i^s and D_i^s are the mass fraction and the diffusion coefficient of component i in the solid phase and $\sum_i c_i^s = 1$.

If one defines a partition coefficient $K_i = c_i^s/c_i$ and assumes chemical equilibrium between the solid and the fluid phases, then previous formulations can be rederived [e.g., *McKenzie*, 1984]. However, since we are interested in nonequilibrium chemical reactions, we shall not follow that practice.

Mass transfer by chemical reaction. Assuming first-order chemical reaction, one can write the rate of mass transfer as

$$\Gamma_i = -R_i A(\mathbf{x}, t)\left[c_i - c_{eq_i}(z)\right], \quad (5)$$

where R_i is the reaction rate constant of component i in kg m^{-2} s^{-1}, A is the specific area (m^2/m^3) available for reaction, and $c_{eq_i}(z)$ is the equilibrium concentration of mineral i in the fluid given in mass fraction.

Solubility is taken to be a linear function of height, as approximately the case for melt that is adiabatically rising [*Sleep*, 1975; *Kelemen et al.*, 1995a]:

$$\frac{\partial c_{eq_i}(z)}{\partial z} = \beta_i, \quad (6)$$

where β_i is a proportionality coefficient describing the steepness of the solubility gradient with units of m^{-1}.

Darcy's law. Darcy's law relates the pressure p and the relative velocity between the fluid and the solid matrix:

$$\phi(\mathbf{v}-\mathbf{V}) = -\frac{k_\phi}{\mu}\nabla p, \tag{7}$$

where the permeability k_ϕ of the porous medium is usually taken to be a power law function of the porosity $k_\phi = d^2\phi^n/b$, with d a typical grain size, n between 2 and 3, and b a constant [e.g., *Turcotte and Schubert*, 1982]. μ is the viscosity of the fluid and p is the pressure in excess of hydrodynamic pressure.

Matrix deformation. The closing equation is the momentum conservation equation which relates pressure changes to the rate of compaction, viscous deformation of the solid phase and body forces acting on the system [*McKenzie*, 1984; *Spiegelman*, 1993a]:

$$\frac{\partial p}{\partial x_i} = \frac{\partial}{\partial x_j}\eta\left(\frac{\partial V_i}{\partial x_j}+\frac{\partial V_j}{\partial x_i}\right) + \frac{\partial}{\partial x_j}(\xi-\frac{2}{3}\eta)\nabla\cdot\mathbf{V} - (1-\phi)\Delta\rho g\delta_{i3}, \tag{8}$$

where η, ξ are the solid phase shear and bulk viscosities and $\Delta\rho = \rho_s - \rho_f$ is the buoyancy difference. Equation (8) states that any change in the pressure field can be expressed as the force the solid exerts on the fluid. In a rigid material where the grain velocity goes to zero ($\mathbf{V} \to 0$), the viscosity of the matrix will go to infinity ($\xi, \eta \to \infty$) and the product will always remain bounded.

The resulting set of dynamical equations are similar to those introduced by workers on compaction of molten rocks [*McKenzie*, 1984; *Spiegelman*, 1993a], but here a specification of a dissolution mechanism (equation (5)) with increasing dissolution as a function of height (equation (6)) brings in interesting behavior. Our goal is to study the combined effect of dissolution and porous flow, rather than to concentrate on the compaction effects.

Simplified Equations

For simplicity, we assume the existence of a fully soluble solid phase composed solely of one mineral ($c^s = 1$) which can chemically react with the fluid by dissolution or precipitation, with first-order kinetics. Since only one reacting component is present, the subscript i will be dropped from here on. The fluid phase is composed of a carrier fluid with mass fraction $1-c$. The carrier fluid component does not enter the solid phase. The dissolved mineral has mass fraction c and effective reaction rate $R_{\text{eff}} = RA$, where we assume that reactive surface area can be taken as constant to leading orders.

The density of the fluid phase is presumed constant as the composition of the melt changes due to chemical reaction. This assumption is approximately correct during dissolution reactions involving basaltic melt and mantle minerals. The solid phase density in a one component system is also a constant.

Neglecting matrix shear, the momentum conservation equation (8) is

$$\nabla p = (\xi+\frac{4}{3}\eta)\nabla C - (1-\phi)\Delta\rho g\hat{k}, \tag{9}$$

where we have defined a compaction rate as $C = \nabla\cdot V$ and $\hat{k}$ is a unit vector in the vertical direction.

Equations (1)-(5) and (7) can now be written as

$$\frac{\partial\phi}{\partial t} + \mathbf{V}\cdot\nabla\phi = (1-\phi)C - R_{\text{eff}}(c - c_{\text{eq}}(z))/\rho_s, \tag{10}$$

$$\frac{\partial\phi}{\partial t} + \nabla\cdot(\mathbf{v}\phi) = -R_{\text{eff}}(c - c_{\text{eq}}(z))/\rho_f, \tag{11}$$

$$\phi\frac{\partial c}{\partial t} + \phi\mathbf{v}\cdot\nabla c = D\nabla\cdot(\phi\nabla c) - (1-c)R_{\text{eff}}(c - c_{\text{eq}}(z))/\rho_f, \tag{12}$$

$$-\phi(\mathbf{v}-\mathbf{V}) = \frac{k_\phi}{\mu}\left[(\xi+\frac{4}{3}\eta)\nabla C - (1-\phi)\Delta\rho g\hat{k}\right], \tag{13}$$

where (12) is a result of subtracting (2) from (3), equation (4) is identical to (1) in the case of $c^s = 1$ and equation (13) is a result of substituting (9) in (7).

Boundary conditions. In general, equations (10)–(13) will require five boundary conditions to solve for $\mathbf{v}$, C, ϕ, and c. Mass conservation requires that the flux across a boundary be continuous or balanced by a source or a sink. Flux boundary conditions include impermeable, rigid, or "free flux" boundary conditions. When the boundary is impermeable, the normal flux is zero either because $k_\phi = 0$ or because $\nabla p\cdot\hat{n} = 0$, where $\hat{n}$ is the direction normal to the boundary. The latter condition poses constraints on $\nabla C\cdot\hat{n}$. At a rigid boundary $C = 0$, and so in the absence of dissolution and matrix flow, a rigid boundary has also a constant porosity (equation (10)). Finally, a free-flux boundary has $\nabla C\cdot\hat{n} = 0$ and yields no resistance to volume changes for the normal flux. In addition to the total flux boundary conditions, mass conservation poses constraints on flux of individual components in the fluid. These constraints translate to specification of concentration of solute in incoming or outgoing fluid.

Nondimensionalization. In nondimensionalizing equations (10)-(13) we shall use the following definitions: Assuming zero solubility at $z = 0$, from (6),

$$c_{\text{eq}}(z) = \beta z.$$

The change in solubility of the matrix between the bottom and top of a box of size L is defined as $c_\delta = c_{\text{eq}}(L) - c_{\text{eq}}(0)$, and so

$$c_\delta = L\beta. \tag{14}$$

The only imposed parameter value in (14) is β, the solubility gradient, known from thermodynamic calculations to be of the order of 2×10^{-6} m^{-1} (an account of calculations made by *Kelemen et al.* [1995a] is given in Appendix A). If we choose to investigate a small-scale box, then c_δ, the change in solubility across the box, will be small as well; $c_\delta \approx 0.2$ over the vertical extant of decompression melting, roughly the upper 75 km of Earth's mantle beneath oceanic spreading ridges. Correspondingly over 100 m, c_δ is of order 10^{-3}.

Porosity is nondimensionalized to a characteristic value, ϕ_0, of the order of 10^{-2} in the partially molten upper mantle beneath spreading ridges [e.g., *Johnson and Dick*, 1992; *Sobolev and Shimizu*, 1993],

$$\phi = \phi_0 \phi'.$$

Permeability is non-dimensionalized to this porosity

$$k_0 = d^2 \phi_0^n / b.$$

Fluid velocity is characterized to be of the order of velocity driven by gravity forces such that

$$\phi_0 w_0 = \frac{k_0}{\mu} \Delta \rho g.$$

Characteristic solid velocity is taken as

$$V_0 = \phi_0 w_0 c_\delta.$$

Finally, we define a compaction length h to be

$$h^2 = \frac{k_0}{\mu}(\xi + 4\eta/3),$$

where $h \to 0$ is an infinitely weak matrix, which compacts instantly, and $h \to \infty$ is a rigid medium; h has a typical value of 100-1000 m in the mantle [*McKenzie*, 1984].

The nondimensional variables will be denoted by primed letters:

$$\begin{aligned} (x, z) &= L(x', z') \\ t &= \frac{L}{w_0 c_\delta} t' \\ C &= \frac{V_0}{L} C' \\ v &= w_0 v' \\ V &= V_0 V' \\ c &= c_\delta c' \\ c_{\text{eq}} &= c_\delta z' \end{aligned}$$

Where the fact that time is scaled to $1/c_\delta$ is a result of our choice to scale time to the characteristic time for change in porosity due to dissolution. In the limit of no gradient of solubility (and thus no dissolution), $c_\delta \to 0$, and the characteristic timescale for change in porosity due to dissolution goes to infinity.

We now write the nondimensional equations:

$$\frac{\partial \phi'}{\partial t} + \phi_0 \mathbf{V}' \cdot \nabla \phi' = (1 - \phi_0 \phi') C' - Da \frac{\rho_f}{\rho_s}(c' - z'), \quad (15)$$

$$c_\delta \frac{\partial \phi'}{\partial t} + \nabla \cdot (\phi' \mathbf{v}') = -c_\delta Da(c' - z'), \quad (16)$$

$$c_\delta \phi' \frac{\partial c'}{\partial t} + \phi' \mathbf{v}' \cdot \nabla c' = -(1 - c_\delta c') Da(c' - z') + \frac{1}{Pe} \nabla \cdot (\phi' \nabla c'), \quad (17)$$

$$\phi'(\mathbf{v}' - \phi_0 \mathbf{V}') = -\phi'^n [\alpha \nabla C' - (1 - \phi_0 \phi') \hat{k}], \quad (18)$$

where Da is defined as advection time across a box versus reaction time:

$$Da = \frac{R_{\text{eff}} L}{\phi_0 w_0 \rho_f}. \quad (19)$$

Alternatively, if we define the "reaction length,"

$$L_{\text{eq}} = \frac{\phi_0 w_0 \rho_f}{R_{\text{eff}}}, \quad (20)$$

to be the length scale over which a perturbation in concentration will equilibrate with the solid matrix if it is traveling at speed w_0, then the Damköhler number is simply the system size in reaction lengths. The reaction length and compaction length are the two inherent length scales in this problem.

The Peclet number is defined as the advection rate versus diffusion rate

$$Pe = \frac{w_0 L}{D}. \quad (21)$$

Finally, we define a rigidity parameter α, which is a combined measure of the change in solubility over one compaction length and the size of a system L relative to a compaction length,

$$\alpha = \frac{h^2}{L^2} \times c_\delta = \frac{h}{L} \times c_h, \quad (22)$$

where $c_h = \beta h$ is the change in solubility over one compaction length. Since L can be as small as we choose, α is not necessarily small even if c_h is small. When $\alpha \to 0$, the matrix is easily compacted, and when $\alpha \to \infty$, the matrix is effectively rigid.

We then neglect all terms of order ϕ_0 (since ϕ_0 is of order of 10^{-2}). The effects of retaining terms of order ϕ_0 when $\phi_0 \ll 1$ have been shown to be small for many problems [*Barcilon and Richter*, 1986; *Scott*, 1988; *Spiegelman*, 1993a]. In addition, we temporarily neglect diffusion, $Pe \to \infty$, so that (15)–(18) become, dropping the primes,

$$\frac{\partial \phi}{\partial t} = C - Da \frac{\rho_f}{\rho_s}(c - z), \quad (23)$$

$$c_\delta \frac{\partial \phi}{\partial t} = -\nabla \cdot (\phi \mathbf{v}) - c_\delta Da(c - z), \quad (24)$$

$$c_\delta \phi \frac{\partial c}{\partial t} = -\phi \mathbf{v} \cdot \nabla c - (1 - c_\delta c) Da(c - z), \quad (25)$$

$$\phi \mathbf{v} = -\phi^n [\alpha \nabla C - \hat{k}]. \quad (26)$$

The value of c_δ increases with system size, but since we are interested in physical systems that have an upper limit in size (the whole region of decompression melting $\approx$ 75 km), c_δ will be less than or equal to the concentration change over that whole region, $c_\delta \leq O(10^{-1})$, and so will be taken here as a small enough parameter to allow for expansion techniques.

Equation (23) tells us that the important timescale in the problem is the timescale over which porosity changes. This happens due to compaction on the one hand and reaction on the other. Equation (24) predicts

that the timescale for divergence of flux is fast compared to that of changing the porosity, since c_δ is a small parameter. Equation (25) predicts that the concentration in the fluid is nearly constant with time. Finally, (26) tells us that pressure gradients will manifest themselves as gradients in compaction rates.

Steady State

We seek unidirectional steady solutions to (23)-(26), of the form

$$[\bar{\phi}(z), \bar{w}(z), \bar{c}(z), \bar{C}(z)] = [\phi^0(z), w^0(z), c^0(z), C^0(z)] + c_\delta[\phi^1(z), w^1(z), c^1(z), C^1(z)], \quad (27)$$

where $\bar{w}(z)$ is the fluid velocity in the z direction, $w^0(z)$ is the zeroth-order solution of the steady state, and $c_\delta w^1(z)$ is a small parameter correction to it; c_δ will be shown to be unimportant in the initial steady state solution but is included here in order to simplify the subsequent linear stability analysis.

Equations (23)-(26) will be solved with a physical picture in mind: at the bottom of the melt column, where melt is entering in equilibrium with its surroundings, there is no dissolution and porosity is constant. Thus we require a "rigid boundary" condition $C = 0$, and a chemical constraint on the concentration field at $z = 0$. These lead to the desired constant porosity at $z = 0$. We also require that fluid flux is continuous across this boundary. Taking into account that only three boundary conditions are needed, now that diffusion of solute and divergence of porosity have been neglected, the boundary conditions take the form of:

$$\bar{\phi}(0) = 1, \quad \bar{w}(0) = 1, \quad \bar{c}(0) = 0. \quad (28)$$

Solutions for the zeroth-order flux are obtained from the fluid conservation equation (24) and the boundary conditions (28)

$$w^0\phi^0 = 1, \quad (29)$$

From the solute concentration equation (25) one then finds that

$$c^0(z) = \frac{1}{Da}(e^{-DaZ} - 1) + z, \quad (30)$$

where $1/Da$ is a measure of the thickness of a boundary layer, i.e., the dimensionless reaction length ($1/Da = L_{eq}/L$).

One can see from (30) that nowhere (except for $z = 0$) does $c^0(z) = z$, the equilibrium value. Rather there is always a deviation of the concentration from the equilibrium concentration, and when the nondimensional height $z \gg L_{eq}/L$, the deviation from equilibrium approaches a constant undersaturation (Figure 2). At any point along the ascent path of the melt, reaction tends to restore the system to equilibrium, but more undersaturated fluid is brought from below to drive the system away from equilibrium. This solution suggests that some degree of disequilibrium will exist as long as the reaction length is significantly larger than the continuum length scale (i.e., the grain scale). When $L_{eq} \leq O(d)$, then the system is effectively in local equilibrium. Note that we will show that the channeling instability arises even under conditions of effectively local equilibrium.

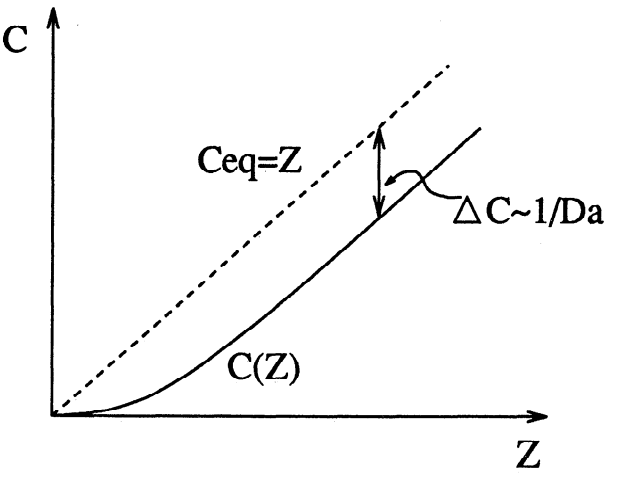

Figure 2. Nondimensional steady state concentration as a function of height, drawn as a solid line. After a narrow boundary layer ($\approx$ 1 reaction length), the deviation of the steady state concentration from the equilibrium value (represented by a dashed line), approaches a constant value $\Delta c \sim 1/Da$.

For simplicity, we shall assume that the nondimensional height is $z \gg L_{eq}/L$ such that any boundary layer effects are negligible. Estimates of the reaction length that are reasonable for Earth are sensitive to assumptions about the microscopic distribution of melt and solid (see Appendix A). For a range of parameters, Table 1 suggests that the equilibration length may range from much less than a millimeter to meters. So even if our system size is of the order of a compaction length, most parameter ranges indicate that significant boundary layers are not expected. Thus we can approximate

$$c^0(z) \approx z - \frac{1}{Da}. \quad (31)$$

The zeroth-order steady state compaction rate is calculated from (23) to be nearly constant for $z \gg L_{eq}/L$

$$C^0(z) = \frac{\rho_f}{\rho_s}(e^{-DaZ} - 1) \approx -\frac{\rho_f}{\rho_s}. \quad (32)$$

From (26) the zero-order steady state porosity is approximately constant:

$$\phi^0(z) = \left(\frac{\rho_f}{\rho_s}\alpha Da\, e^{-DaZ} + 1\right)^{-1/n} \approx 1. \quad (33)$$

Finally, from (29) the velocity is also approximately constant:

$$w^0(z) \approx 1. \quad (34)$$

The zeroth-order steady state of constant porosity and upwelling velocity is sustained by the competition be-

Table 1. Characteristic Values Believed to Be Applicable to Earth's Mantle

Variable	Symbol	Value	Notes
Solubility gradient	β	$2 \times 10^{-6} m^{-1}$	1
Linear dissolution rate		$10^{-12} - 10^{-8}$ m s^{-1}	2
Solid density	ρ_s	3×10^3 kg m^{-3}	
Reaction rate constant	R	$10^{-9} - 10^{-5}$ kg m^{-2} s^{-1}	
Grain edge length	d	$10^{-4} - 10^{-3}$ m	
Total surface area		$10^3 - 10^5$ m^2/m^3	3, using d and cubic grains
Porosity	ϕ	$10^{-3} - 10^{-2}$	4
Solid/liquid surface area	S	$(1-3) \times 10^{-1}$	in fraction of total surface area.
Volume fraction of soluble phase		$10^{-2} - 10^{-1}$	i.e., fraction of pyroxene, 5
Permeability exponent	n	$2 - 3$	3
Melt fraction	F	$0.05 - 0.2$	fraction of solid mass that has melted
Solid upwelling rate	V_0	$10^{-10} - 10^{-9}$ m s^{-1}	
Background fluid velocity	w_0	$10^{-9} - 10^{-6}$ m s^{-1}	see Appendix A
Equilibration length	L_{eq}	$10^{-7} - 10$ m	see Appendix A
Damköhler number (L=100m)	Da	$10^9 - 1$	using range of L_{eq} given above
Diffusion coefficient	D	$10^{-12} - 10^{-10}$ m^2 s^{-1}	6
Peclet number (L=100m)	Pe	$10^8 - 10^3$	using w_0, D
compaction length	h	$100 - 1000$ m	7

For a detailed discussion, see Appendix A. Notes: 1, *Kelemen et al.* [1995a]; *Kelemen and Dick* [1995]. 2, higher dissolution rates are from *Brearley et al.* [1986] and *Kuo and Kirkpatrick* [1985], and low dissolution rate is from *Zhang et al.* [1989]. 3, *VonBargen and Waff* [1986]. 4, *Johnson and Dick* [1992]; *Sobolev and Shimizu* [1993]. 5, *Kelemen et al.* [1992]. 6, *Hofmann* [1980]. 7, *McKenzie* [1984].

tween porosity formed by dissolution and destroyed by compaction. Since compaction rate is the gradient of grain velocity, constant compaction means that grains descend with increasing speed as a function of height, which exactly balances the net increase in dissolution with height.

The c_δ-order terms of the steady state can be easily obtained from (23)-(26) using the zeroth-order solutions and boundary conditions of $\phi^1(0) = w^1(0) = c^1(0) = 0$, but their detail is of no particular interest here, since in the stability analysis perturbations to terms of order c_δ are negligibly small compared to perturbations to terms of order 0.

Linear Analysis

We shall perform a linear stability analysis of (23)-(26) assuming that all variables can be expressed as their steady state value plus small deviations:

$$[\phi'(x,t), w'(x,t), u'(x,t), c'(x,t), C'(x,t)] = [\bar{\phi}(z), \bar{w}(z), 0, \bar{c}(z), \bar{C}(z)] + \epsilon[\hat{\phi}(x,t), \hat{w}(x,t), \hat{u}(x,t), \hat{c}(x,t), \hat{C}(x,t)], \quad (35)$$

where $\epsilon \ll 1$ and the steady state values are defined by (27)-(34).

Keeping $O(\epsilon)$ terms and discarding terms of $O(c_\delta \epsilon, \epsilon^2)$, the perturbation equations take the following form:

$$\frac{\partial \hat{\phi}}{\partial t} = \hat{C} - Da \frac{\rho_f}{\rho_s} \hat{c}, \quad (36)$$

$$0 = \frac{\partial \hat{w}}{\partial z} + \frac{\partial \hat{\phi}}{\partial z} + \frac{\partial \hat{u}}{\partial x}, \quad (37)$$

$$0 = -\hat{\phi} - \hat{w} - \frac{\partial \hat{c}}{\partial z} - Da\hat{c}, \quad (38)$$

$$\hat{w} = (n-1)\hat{\phi} - \alpha \frac{\partial \hat{C}}{\partial z}, \quad (39)$$

$$\hat{u} = -\alpha \frac{\partial \hat{C}}{\partial x}. \quad (40)$$

In solving the perturbation equations (36)-(40) we shall assume that all variables have the form of

$$[\hat{w}(x,t), \hat{u}(x,t), \hat{\phi}(x,t), \hat{c}(x,t), \hat{C}(x,t)] = [\tilde{w}(z), \tilde{u}(z), \tilde{\phi}(z), \tilde{c}(z), \tilde{C}(z)] e^{\sigma t} e^{ilx}, \quad (41)$$

where σ is the nondimensional growth rate of the perturbation and l is the nondimensional wavenumber in the horizontal direction. Equation (38) can be rewritten using (36), (39), and (40) to be a function of $\tilde{\phi}, \tilde{C}$ only

$$\left[nDa\frac{\rho_f}{\rho_s} - \sigma(\mathcal{D} + Da)\right]\tilde{\phi} = \left[(\alpha Da \frac{\rho_f}{\rho_s} - 1)\mathcal{D} - Da\right]\tilde{C}, \quad (42)$$

where $\partial/\partial z$ is designated by the operator symbol $\mathcal{D}$.

Equation (37) can also be rewritten using $\tilde{C}, \tilde{\phi}$:

$$n\mathcal{D}\tilde{\phi} = \alpha(\mathcal{D}^2 - l^2)\tilde{C}, \quad (43)$$

eliminating $\tilde{\phi}$ from both of these equations, one arrives at a final equation for a single variable

$$[\alpha\sigma\mathcal{D}^3 + (\alpha\sigma Da - n)\mathcal{D}^2 - (l^2\alpha\sigma + nDa)\mathcal{D} + \alpha l^2 Da(n\rho_f/\rho_s - \sigma)]\,\tilde{C} = 0. \quad (44)$$

Preview of Solutions and a Simple Scaling Argument

There are two kinds of instabilities that we find in this system: One is the growth of an absolute instability, which is stationary in space and obeys a set of boundary conditions. In this case the growth rate σ is purely real and so dissolution features will grow pinned in space and will not travel. The other kind of instability is growth in time of the amplitude of traveling waves (in this case, σ is complex), in which we assume a semi-infinite medium and investigate the behavior of traveling waves without imposing boundary or initial conditions (these can be imposed in a future investigation in order to study the effects of the finite size of the medium on the unstable wave solutions).

How do we expect the most unstable wavelength of the absolute instability to behave as we change Da, the control parameter, and should we expect a dominant wavelength to emerge at all? As a perturbation of horizontal wavelength λ_x grows, unsaturated fluid converges laterally toward growing features: when there is no diffusion (for discussion of diffusion effects, see Appendix B) and only reaction is present to counteract the deviations from equilibrium, we expect that if the time to advect laterally across a perturbation (λ_x/u) is longer than time for reaction to wipe out the concentration difference ($1/R_{\text{eff}}$), then the perturbation will not focus enough unsaturated fluid to keep itself alive and it will be damped. This means that perturbations with long horizontal wavelengths compared to L_{eq} will not grow effectively. On the other hand, focusing by the longest of the fast growing wavelengths will starve the shorter ones, and a dominant horizontal wavelength is expected to emerge. By this argument, the horizontal wavelength of the most unstable mode should increase with increasing L_{eq} (decreasing Da number).

Compaction is expected to damp horizontal wavelengths comparable to a compaction length. We propose that if L_{eq} is so large that that the most unstable wavelength is of the order of a compaction length, then stationary channels could not be maintained in the system. However, the results of our study indicate that even when stationary channels are inhibited from growth, the system still exhibits a "traveling instability": unstable growth of traveling waves.

Unstable Stationary Channels

In this section we investigate the growth of unstable dissolution features by investigating the growth rate of vertical modes that obey boundary conditions, termed "absolute instability."

A solution to (44) of the form

$$\tilde{C}(z) = A_1 e^{m_1 z} + A_2 e^{m_2 z} + A_3 e^{m_3 z} \quad (45)$$

will exist, provided that

$$m^3 + (Da - \frac{n}{\alpha\sigma})m^2 - (l^2 + \frac{nDa}{\alpha\sigma})m + l^2 Da(\frac{n\rho_f}{\rho_s\sigma} - 1) = 0, \quad (46)$$

where $m_{1,2,3}$, the three roots of the cubic polynomial (46), are either all real or one real and two complex conjugates. Equation (46) establishes the relationship between wavenumbers in the vertical (m_1, m_2, m_3) and horizontal (l) directions and their growth rate. In order to find the solution of the linear stability problem (that is, to find the growth rate σ as a function of the Damkholer number and the rigidity α for any given horizontal wavenumber l) we need to specify a set of three boundary conditions, which actually correspond to the third-order differential equation (44). These boundary conditions will constrain the vertical modes m_1, m_2 and m_3, and as a consequence determine $\sigma(l, Da, \alpha)$ via (46).

Boundary conditions for equation (44) emerge from the following assumptions: (1) There is no dissolution and porosity is constant at $z = 0$, where the incoming fluid is in equilibrium with the matrix. This assumption leads, via (36), to a rigid boundary condition ($C = 0$) at $z = 0$. (2) The $z = 0$ boundary is impermeable to the perturbation, meaning that the flux of fluid normal to the boundary remains unperturbed from its steady state value. (3) Using an observation from physical and computer experiments [*Kelemen et al.*, 1995a] that lateral fluxes ahead of the perturbation are negligible, we require (from (40)) a rigid boundary at $z = L$ as well. (Alternatively, one could choose a "free-flux" boundary at $z = L$, which actually acts to amplify the perturbation by relaxing the restrictive top rigid-boundary condition, and also complicates the mathematical presentation somewhat.) The above conditions are equivalent to

$$\tilde{C}(z=0) = 0, \quad \tilde{C}(z=1) = 0, \quad \frac{\partial\tilde{C}}{\partial z}(z=0) = 0, \quad (47)$$

and we seek the conditions under which a nontrivial solution of the form (45) exists.

The boundary conditions (47) tell us that

$$\begin{pmatrix} 1 & 1 & 1 \\ e^{m_1} & e^{m_2} & e^{m_3} \\ m_1 & m_2 & m_3 \end{pmatrix} \begin{pmatrix} A_1 \\ A_2 \\ A_3 \end{pmatrix} = \begin{pmatrix} 0 \\ 0 \\ 0 \end{pmatrix}. \quad (48)$$

This has a nontrivial solution if the determinant is equal to zero:

$$e^{m_1}(m_2 - m_3) + e^{m_2}(m_3 - m_1) + e^{m_3}(m_1 - m_2) = 0. \quad (49)$$

To find the growth rate as a function of horizontal wavenumber from (46) and (49), we first analytically calculate the three roots $m_{1,2,3}(\sigma, l, Da, \alpha)$ of the cubic polynomial (46). Substituting these roots into (49), we then obtain an implicit equation for $\sigma(l, Da, \alpha)$. Choosing a value for the parameters Da and α, we finally obtain $\sigma(l)$ by seeking the roots of the implicit equation (49), using a bisection numerical method. Numerical solutions indicate that m_1, m_2, m_3 have the form of 1 real root and 2 complex conjugates so that $\tilde{C}(z)$ of (45) can be written as

$$\tilde{C}(z) = B_1 e^{m_1 z} + B_2 e^{pz} \cos qz + B_3 e^{pz} \sin qz. \quad (50)$$

Before presenting the results of the linear stability analysis, we would like to briefly discuss the physics of the problem revealed by writing (46) as a dispersion relation in which $\sigma = \sigma(m, l)$:

$$\sigma = \frac{1}{\alpha} \frac{nm}{m^2 - l^2} - \frac{nl^2 Da \frac{\rho_f}{\rho_s}}{(m^2 - l^2)(m + Da)}. \quad (51)$$

The growth rate σ is composed of two completely separate parts, one that includes a dependence on the rigidity of the matrix, α, but does not depend on the chemical reaction, and the second that depends only on the rate of chemical reactions, the Da number, but does not depend on the rigidity; σ can be expressed as a sum of these parts

$$\sigma = \sigma_C + \sigma_{Da}, \quad (52)$$

where the compaction contribution to the growth rate is

$$\sigma_C = \frac{1}{\alpha} \frac{nm}{(m^2 - l^2)} \quad (53)$$

and the chemical reaction contribution to the growth rate is

$$\sigma_{Da} = -\frac{nl^2 Da \frac{\rho_f}{\rho_s}}{(m^2 - l^2)(m + Da)}. \quad (54)$$

As the matrix rigidity is increased ($\alpha \to \infty$), then $\sigma \to \sigma_{Da}$. This limit strips away compaction effects on the instability. In the limit of $Da \to 0$, $\sigma \to \sigma_C$ and only compaction effects are left.

Rigid medium limit. As mentioned previously, in the limit of a rigid medium ($1/\alpha \to 0$), compaction effects are not present, illuminating the physics of the dissolution instability. In Figure 3 we present the growth rate σ as a function of the horizontal wavenumber l for $Da = 10$ in a rigid medium ($1/\alpha = 0$). For comparison, the growth rate in a compacting medium with $\alpha = 1$ is also shown. The choice of $Da = 10$ is given as an example, to demonstrate the qualitative behavior of the solution. For a rigid medium any value of Da produces the same kind of behavior with positive growth rate peaking at a certain wavelength. Results for a compacting medium will be discussed in the next section.

It should be noted that actually σ attains several values for each value of l: these correspond to different growth rates of different vertical modes with a wavelength $\lambda_z = 2\pi/q$ where q is defined in (50). The first mode has approximately half a wavelength (q close to π) in the vertical dimension of the box and is the fastest growing mode. The second mode has close to one wavelength fitted in the vertical dimension and grows more slowly. The third mode grows even more slowly, etc. Hence only the first mode, the fastest growing one, is plotted on Figure 3. The growth rate in Figure 3 is seen to peak for horizontal wavenumber $l_{\max}$, and so $\lambda_x = 2\pi/l_{\max}$ is the most unstable wavelength in the system.

Calculations similar to Figure 3 have been made for different Da numbers. Figure 4a shows the most unstable wavelengths, λ_x, as a function of Da, for the rigid medium case. As Da increases, λ_x is shown to decrease and to approach a power law dependence on Da. For $Da \gg 1$, and spanning 4 orders of magnitude, the nondimensional dominant horizontal wavelength scales as $\lambda_x' \sim \sqrt{1/Da}$. In dimensional units this means that

$$\lambda_x \sim \sqrt{L * L_{\text{eq}}}. \quad (55)$$

The increase in dominant horizontal wavelengths of channels with increasing equilibration length (decreasing Da) is as predicted by the "preview of solutions." The fact that the lateral extent of channels depends also on the vertical dimension of the box is more surprising. We postulate that the vertical length scale L is imposed on the perturbations by the fact that channels always span the box vertically. Since the vertical mode is coupled to the horizontal modes in (46), the horizontal modes are forced to feel the system size too. The aspect ratio (λ_x/λ_z) of the channels decreases as Da is increased. Since in dimensional parameters (when $Da \gg 1$) $\lambda_z \sim L$ and $\lambda_x \sim \sqrt{L * L_{\text{eq}}}$, then the aspect ratio is

$$\lambda_x/\lambda_z \sim \sqrt{L_{\text{eq}}/L} = \sqrt{1/Da}, \quad (56)$$

as seen in Figure 4b, and the channels become more

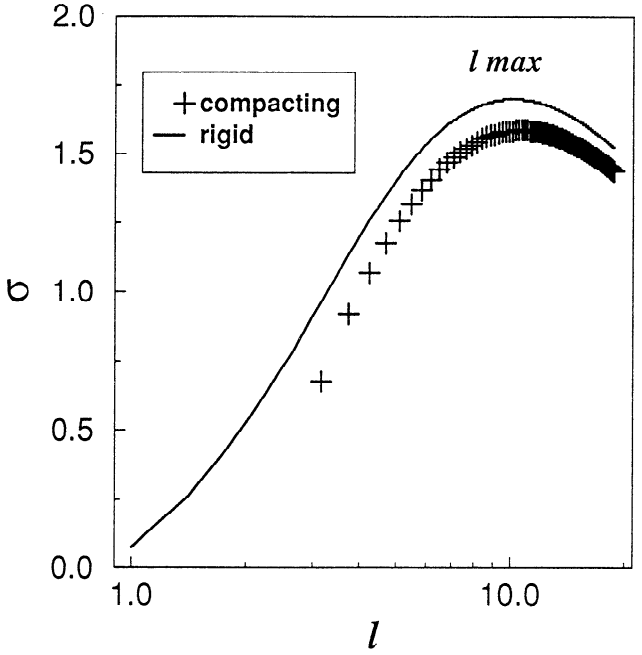

Figure 3. Nondimensional growth rate σ versus nondimensional horizontal wavenumber l, for $Da = 10$ in a rigid medium ($1/\alpha = 0$), and in a compacting medium with $\alpha = 1$; $l_{\max}$ indicates the fastest growing wavenumber. Comparing the growth of unstable channels in a compacting and a rigid medium, one notes that the most unstable wavelength is hardly altered and its growth rate is only slightly lowered due to the stabilizing effect of compaction. Compaction does, however, damp the long-wavelength perturbations. This effect leads to a critical Da for existence of the instability in a compacting medium.

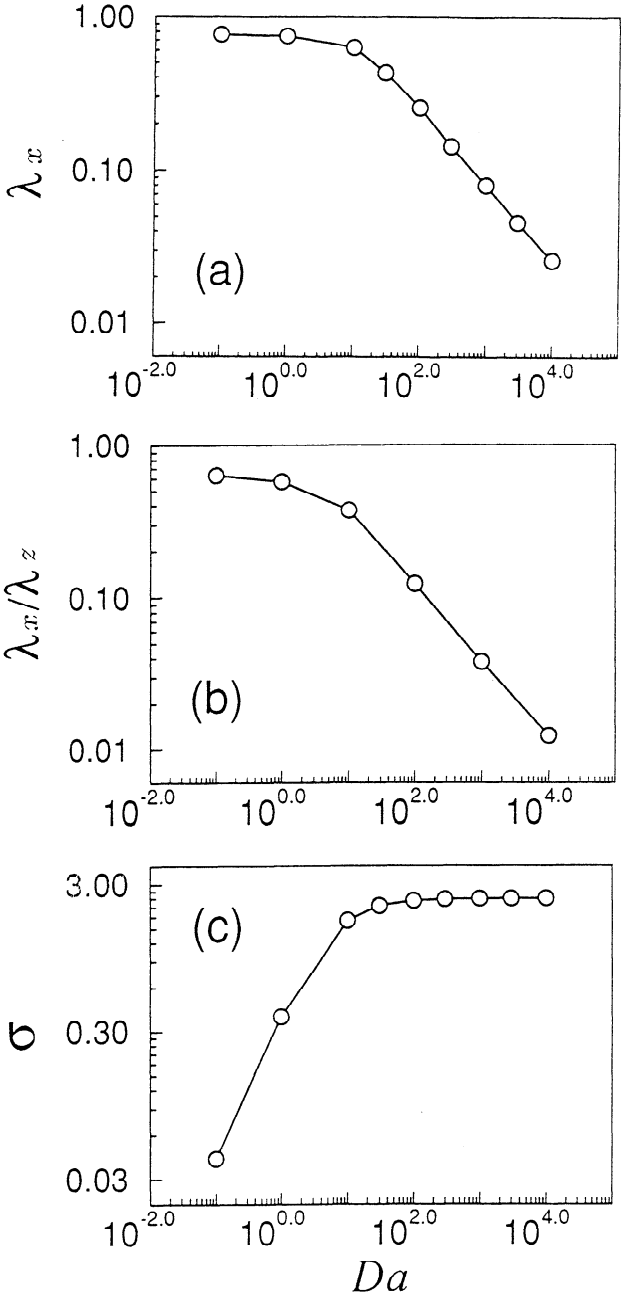

Figure 4. (a) The fastest growing horizontal wavelength, $\lambda_x = 2\pi/l_{\max}$, derived from plots similar to Figure 3 with different Da numbers in a rigid medium. For $Da > 1$, and spanning 4 orders of magnitude, $\lambda_x^2 \propto 1/Da$. (b) Aspect ratio of channels, $q/l = \lambda_x/\lambda_z$, as a function of Da in a rigid medium. Perturbations become more finger like as Da number is increased. (c) Growth rate of $l_{\max}$ as a function of Da in a rigid medium. The system becomes increasingly unstable with increase in Da and reaches a constant limit for $Da \to \infty$. This limit is set by the derivative of permeability with respect to porosity.

finger-like as the equilibration length decreases or as the system size increases.

The growth rate σ of the fastest growing horizontal wavenumber $l_{\max}$ as a function of Da is plotted in Figure 4c, where one can see that as $Da \to \infty$, the growth rate approaches a constant value, $\sigma \to n\rho_f/\rho_s$, which can be predicted from (54). This limit is determined by $\partial k/\partial\phi \propto n$, the derivative of the permeability with respect to porosity. If the permeability decreased with increasing porosity, then the instability would not occur and the growth rate would approach a negative constant value. In other words, the maximum change in porosity is only related to the rate at which flux changes with porosity.

The increase of σ with Da seems counterintuitive at first, since as Da is increased the system is closer to equilibrium (equation (31) and Figure 2). The explanation stems from the fact that as $Da \to \infty$, any perturbation in flux is immediately compensated by chemical reaction bringing the liquid close to local chemical equilibrium. In the meantime, the porosity has been lowered further by the strong dissolution, so additional fluid flows into the perturbed region. This in turn will result in immediate strong dissolution lowering the porosity even further. On the other hand, a low Da number will tend to weaken the growth of channels because the fluid has time to redistribute the concentration by lateral advection and thus smooth away gradients before substantial dissolution occurs.

Compacting medium. Numerical solutions for a compacting medium with α of order 1 indicate that there exists a critical value for Da. For

$$Da > Da_{\text{crit}} = 1/\alpha, \tag{57}$$

dissolution channels will grow. Once condition (57) is violated, there are no solutions which obey the boundary conditions (47) and dissolution channels do not form.

Condition (57) can be rewritten using the definitions of Da, α and L (equations (19), (22), and (14)):

$$Da\,\alpha = c_h \frac{h}{L_{\text{eq}}} > 1. \tag{58}$$

In other words, this term is proportional to the ratio of the compaction length to the reaction length. If the compaction length is much larger than the reaction length, permanent channels can grow. Otherwise, compaction will become important and will act as a stabilising mechanism, trying to squeeze the channels shut and forcing propagation of the instability as waves, as can be seen in the "unstable dissolution waves" section.

Figure 3 shows the growth rate for $Da = 10, \alpha = 1$, so that $Da\,\alpha = 10$, not so high above the critical value and in the lower range of values of $Da \times \alpha$ predicted for the mantle, as can be seen in Table 1. Growth rates in a compacting medium are shown in comparison with results for $Da = 10$ and a rigid medium, $1/\alpha = 0$. Figure 3 shows that the maximum wavelength in the compacting medium is not changed from a completely rigid medium and the growth rate is only slightly lower than in the rigid case. Compaction is shown to damp the long wavelengths, as expected.

Eigenfunctions. Here we calculate the eigenfunctions (full z dependent solutions) of all perturbed fields in the problem $(\hat{C}, \hat{\phi}, \hat{u}, \hat{v}, \hat{c})$ and plot them as contour plots, taking a snapshot in time. This demonstrates our claim that the instability is characterized by channel-like features and helps one to visualize the spatial distribution of melt and porosity.

We use (50), the three independent boundary conditions (47), and (36)-(41) to analytically find the eigenfunctions and thus the full solutions for the perturbation variables:

$$\hat{C}(x,z,t) = B_1 \left[\frac{m_1 - p}{q} e^{pz} \sin qz + e^{pz} \cos qz - e^{m_1 z} \right] e^{ilx+\sigma t} \tag{59}$$

$$\hat{\phi}(x,z,t) = B_1 \frac{\alpha}{n} \left[\left(\frac{q(q^2+2p^2+l^2-m_1 p)}{p^2+q^2} - \frac{p(m_1-p)(p^2-l^2)}{q(p^2+q^2)} \right) e^{pz} \sin qz + \frac{2pl^2 - m_1(p^2+q^2+l^2)}{p^2+q^2} e^{pz} \cos qz + \frac{m_1^2 - l^2}{m_1} e^{m_1 z} + l^2 \left(\frac{m_1 - 2p}{p^2+q^2} + \frac{1}{m_1} \right) \right] e^{ilx+\sigma t} \tag{60}$$

$$\hat{u}(x,z,t) = -iB_1 \alpha l \hat{C} \tag{61}$$

$$\hat{w}(x,z,t) = (n-1)\hat{\phi} + B_1 \frac{\alpha}{q} \left[((m_1 - p)p - q^2) e^{pz} \cdot \sin qz + m_1 q (e^{pz} \cos qz - e^{m_1 z}) \right] e^{ilx+\sigma t} \tag{62}$$

$$\hat{c}(x,z,t) = \frac{\rho_s}{\rho_f Da} \left[\hat{C} - \hat{\phi} \cdot \left(\frac{1}{\alpha} \frac{nm_1}{m_1^2 - l^2} - \frac{n\rho_f l^2 Da}{\rho_s (m_1^2 - l^2)(m_1 + Da)} \right) \right] \tag{63}$$

In order to plot the behavior of the perturbation variables as a function of x and z, we use the values of m_1, p, q, and σ calculated numerically for the most unstable wavelength, as described in the previous section. In the surface plots illustrated in Figure 5 we used parameter values of $Da = 100, \alpha = 1$.

Figure 5a is a plot of the perturbation in compaction $\hat{C}(x,z,t_0)$, which is equivalent to the perturbation pressure. Narrow channels spanning the vertical dimension of the box can be seen. The constant pressure boundary conditions force the pressure field to achieve a maximum at about three quarters of the way to the top of the box and not at the top boundary. Porosity $\hat{\phi}(x,z,t_0)$ is plotted in Figure 5b and can be seen to have increasing amplitude with increasing height and to achieve a maximum amplitude at the top of the box. Disequilibrium undersaturation, $-\hat{c}(x,z,t_0)$, and vertical velocity

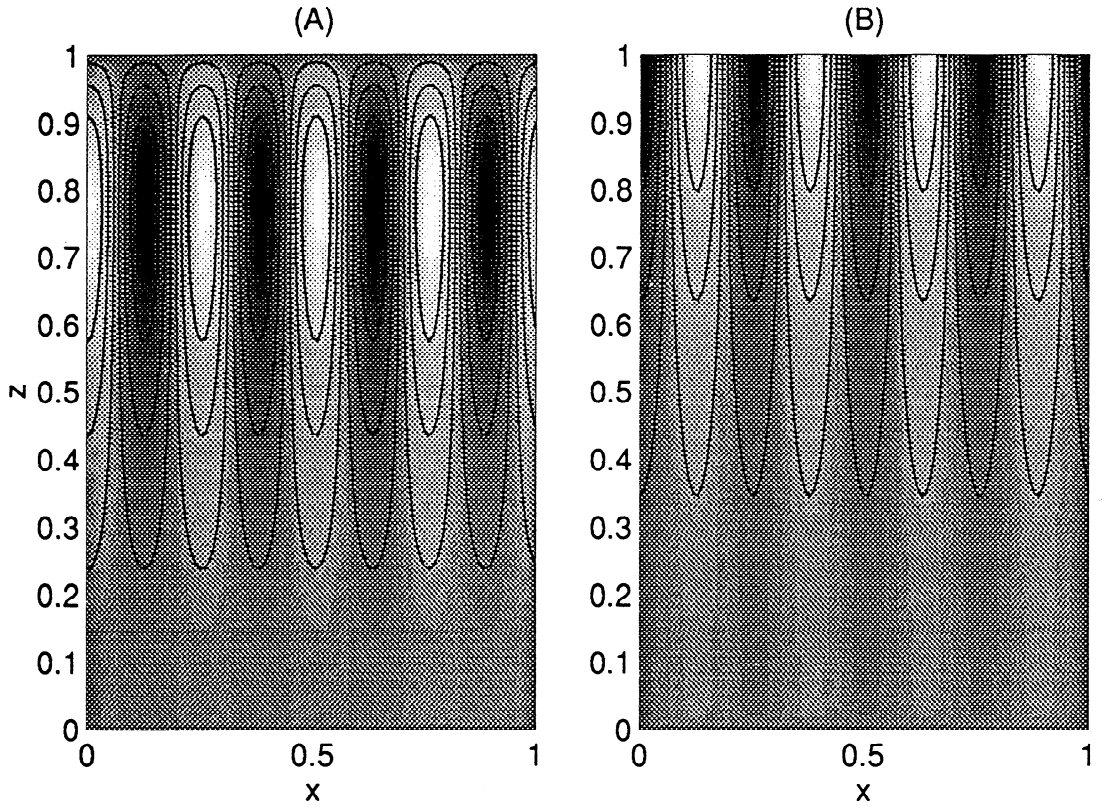

Figure 5. Eigenfunctions for a compacting medium, $Da = 10, \alpha = 1$ (a) Perturbation pressure as a function of x and z. Dark shading indicates negative values; light shadings indicate positive values. Owing to the boundary conditions, pressure perturbations are forced to zero at the top of the box, thus attaining a maximum amplitude at $z \approx 3/4$. (b) Porosity, vertical velocity, and concentration, which look very similar, are plotted as a function of x and z. These variables have increasing amplitude as a function of z and attain a maximum at $z = 1$.

have surface plots very similar in shape to the plot of porosity.

Within linear approximations, when the system is unstable, the longer the melt ascends, the more robust the instability becomes, spanning any given box size. This is understandable, since the more disequilibrated the ascending fluid, the stronger the driving force for instability.

Unstable Dissolution Waves

In this section we present a different solution to the set of perturbation equations (36)-(40), which is independent of the channel solution and may coexist with it. We study simple linear propagating waves in an infinite medium. These are related to compaction waves but present a previously unstudied facet of the RII instability, unstable traveling dissolution waves.

When mass transfer between the solid and the liquid is zero ($Da = 0$), equations (36)-(40) are close to the ones arrived by *Spiegelman* [1993a] in his linear analysis of compaction driven waves, apart from another time derivative which survived in his divergence equation because of the different time scales and therefore different linearization involved. In the limit of $Da \to 0$ we arrive at an equation for traveling waves:

$$n\frac{\partial \phi}{\partial z} - \nabla^2 \frac{\partial \phi}{\partial t} = 0. \tag{64}$$

Assuming wave solutions of the form

$$\phi = Ae^{i(lx+mz-\sigma t)}, \tag{65}$$

the dispersion relation is

$$\sigma = \frac{nm}{m^2+l^2}, \tag{66}$$

indicating the existence of traveling waves, with a phase velocity c_p

$$c_p = \frac{\sigma}{K} = \frac{n\cos\theta}{K^2}, \tag{67}$$

where the wave vector is defined by $K^2 = l^2 + m^2$ and θ is the angle between the wave vector and the vertical, as seen in Figure 6a. The phase velocity in the z direction, $c_{pz} = c_p/\cos\theta$, is greater than zero, thus linear compaction waves always travel with an upward component. (It is interesting to note that (64) is identical to the equation for planetary Rossby waves that dominate the ocean and atmosphere. Rossby waves have westward traveling phases.)

These results from the zero Da limit are close to the results from *Spiegelman* [1993a], in which traveling dispersive waves arise from compaction. The waves form due to the increase of melt flux as a function of porosity, and its ability to deform the matrix. Viscous resistance to volume change causes waves to disperse.

We now turn to study the full problem of nonzero Da and seek wave-like solutions to the set of perturbation equations (36)-(40),

$$\hat{C}(z,x,t) \sim e^{i(mz+lx)+\sigma t},$$

where m and l are real and σ is to be determined from the dispersion relation. A single equation similar to (46) is found, which in turn can be written as a dispersion relation that restricts the growth rate to be

$$\sigma = \frac{nl^2Da^2\frac{\rho_f}{\rho_s}}{(m^2+l^2)(m^2+Da^2)} - in\frac{m}{m^2+l^2}\left[\frac{1}{\alpha} + \frac{\rho_f l^2 Da}{\rho_s(m^2+Da^2)}\right]. \tag{68}$$

This growth rate has an imaginary part, $\sigma_{\mathcal{I}}$, and a real positive part, $\sigma_{\mathcal{R}}$, indicating that if porosity waves were formed in the presence of dissolution, their amplitude would increase with time to form "unstable traveling dissolution waves", or "channelleons".

The phase velocity of the waves, c_p, is

$$c_p = -\frac{\sigma_{\mathcal{I}}}{K} = n\cos\theta\left(\frac{1}{\alpha K^2} + \frac{\sin^2\theta Da\frac{\rho_f}{\rho_s}}{K^2\cos^2\theta + Da^2}\right). \tag{69}$$

where the wave vector is defined by $K^2 = l^2+m^2$ and θ is the angle between the wave vector and the vertical. In the presence of dissolution, the amplitude of the waves grows in time due to the positive real part of the growth rate,

$$\sigma_{\mathcal{R}} = \frac{n\sin^2\theta Da^2\frac{\rho_f}{\rho_s}}{K^2\cos^2\theta + Da^2}. \tag{70}$$

Here $\sigma_{\mathcal{R}}$ is seen to be always positive, providing a mechanism for nucleation and growth of "magmons", which previously required an initial step perturbation in porosity in order to nucleate. For $Da = 0$, $\sigma_{\mathcal{R}} = 0$, indicating that compaction waves in the absence of dissolution are marginally stable and travel with a constant amplitude.

The presence of dissolution ($Da > 0$) brings about interesting behavior of both the phase velocity of the waves and the rate at which their amplitude grows. Figure 6b illustrates c_p and $\sigma_{\mathcal{R}}$ as calculated from (69) and (70). The top panel shows c_p and $\sigma_{\mathcal{R}}$ as a function of orientation of the wave front θ for constant K, Da, and α. The phase velocity of planar waves is maximal when they have a diagonal orientation but drops to zero for waves that are oriented vertically ($\theta \to \pi/2$). On the other hand, these vertical "stationary channels" are the ones that grow the fastest, as is seen from $\sigma(\theta)$, and are actually the collapse of the traveling wave solution to the stationary channel solution obtained in the previous section. The bottom panel of Figure 6B shows c_p and $\sigma_{\mathcal{R}}$ as a function of Da for constant K, θ, and α. The maximum in phase velocity corresponds to $K\cos\theta = Da$, while maximal growth rate occurs for $Da \to \infty$, similar to the maximal growth rate for the stationary channels. Compaction-dissolution waves are dispersive, as expected for waves which arise partly from compaction [*Spiegelman*, 1993a], and the long wavelengths both travel and grow the fastest. Like the lin-

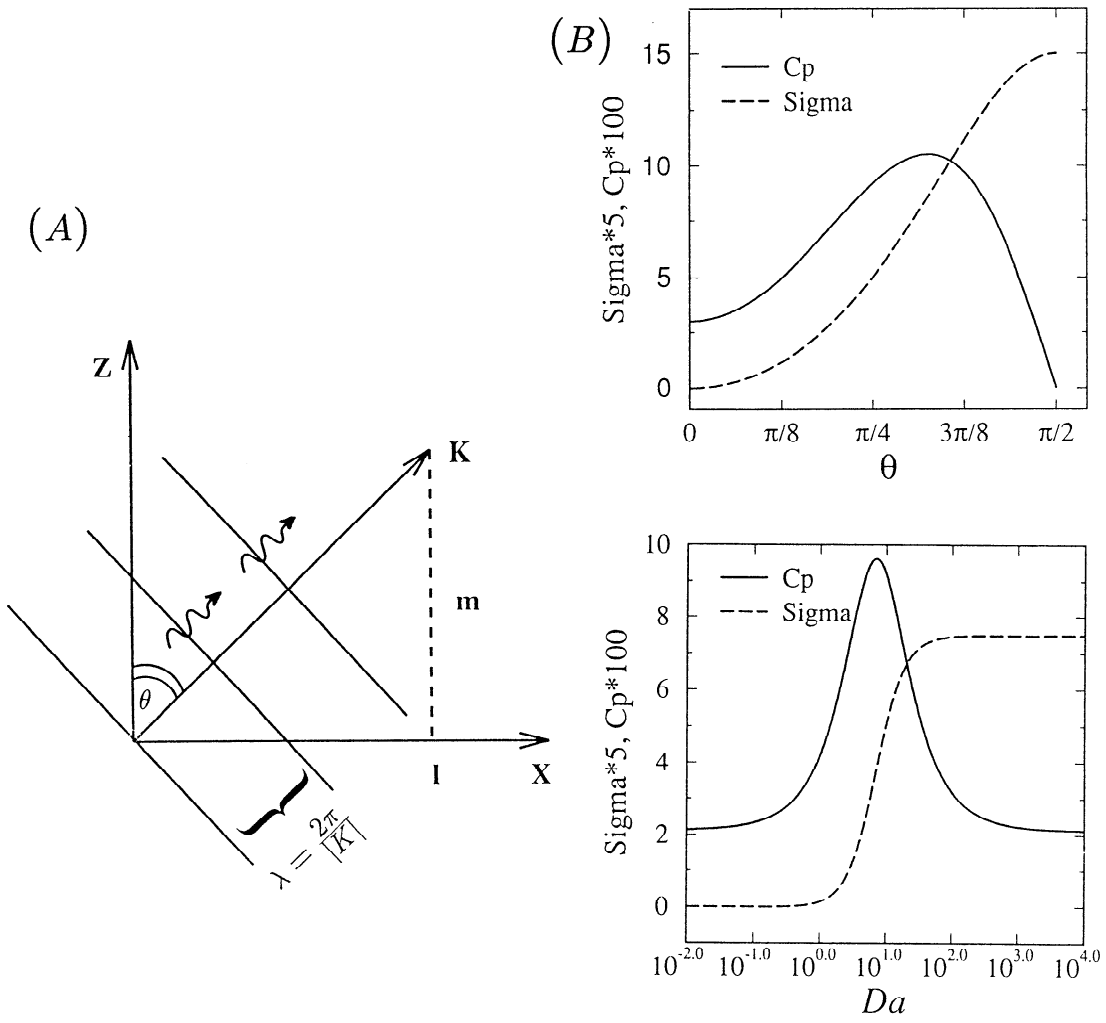

Figure 6. (a) Schematic drawing of a planar wave, with wave vector $K^2 = l^2 + m^2$, oriented at angle θ to the vertical. The phase velocity is the velocity at which the phases propagate. (b) (top) Growth rate $\sigma_{\mathcal{R}}$ and phase velocity c_p of compaction-dissolution waves as a function of the planar wave orientation θ. Calculations were made using $K = 10$, $Da = 10$, and $\alpha = 1$. Phase velocity is maximum when the wave is at some angle to the vertical and is zero for vertical stripes. Although these stripes do not propagate, they grow the most rapidly, as seen from $\sigma(\theta)$. The stationary vertical stripes are the collapse of the plane wave solution to the unstable channels solution. (bottom) The $\sigma_{\mathcal{R}}$ and c_p as a function of Da. Calculations were made using $K = 10$, $\theta = \pi/4$ and $\alpha = 1$. The maximum in phase velocity is for waves with $K \cos\theta = Da$. At this point a rapid transition from nearly zero growth rate to maximum growth rate can be observed.

ear compaction waves of (64), these waves always have an upward phase velocity. Waves propagate with a finite phase velocity even in the absence of compaction. They appear to travel diagonally because vertical wavelengths that are shorter than the system size ($m > 0$ or $\theta < \pi/2$) imply that at some point in space, upwelling fluids in high-porosity regions encounter an obstacle of low porosity, forcing the fluid to chew its way up with a diagonal component of velocity.

Discussion

The results of this work show the potential for an existence of a channeling instability in Earth's upper mantle. The instability stems from combined chemical and hydrodynamical effects. Melt decompresses as it ascends through the mantle, increasing its ability to dissolve the surrounding matrix. A small perturbation in porosity allows a larger volume of unsaturated fluid to flow, thus increasing dissolution and further increasing porosity in a positive feedback mechanism.

We consider a model system incorporating porous flow, dissolution, and matrix compaction effects and find a steady state formed by the competition between dissolution and compaction. Linear stability analysis is then performed, predicting that long, narrow channels may spontaneously form. The emerging horizontal wavelength λ_x is shown to depend on the chemical equilibration length L_{eq} and the vertical extent of the system L. For chemical equilibration lengths

that are smaller than the size of the system ($Da > 1$), $\lambda_z = 2.534\sqrt{L_{eq}L}$. For a system of the size of the melting region, $L \approx 75$ km, channels will range from 10 cm wide, when $L_{eq} \sim 10^{-7}$ m, to nearly a kilometer wide if $L_{eq} \sim 10$ m. Our linear prediction of channel width is in agreement with (1) postulated vein sizes needed to successfully segregate the melt in order to see observed chemical signatures [*Spiegelman and Kenyon*, 1992], and (2) the size of dunite dissolution features found in field observations [*Boudier and Nicolas*, 1977; *Dick*, 1977; *Quick*, 1981; *Nicolas*, 1989; *Kelemen et al.*, 1992]. This further strengthens our belief that the channeling instability plays a crucial role in focusing of melt and determining the geochemical composition of upwelling liquids and residual mantle peridotites. Channels formed by the reactive infiltration instability may provide the means for extracting melt out of the viscously deformable upper mantle.

If the chemical equilibration length is too long, comparable to the compaction length, formation of the instability is inhibited by compaction. A coexisting solution predicts unstable growth of elongated traveling porosity and concentration waves that exist under all conditions. The exact criterion for stationary channels to grow is $c_h h/L_{eq} > 1$. We test whether this condition is met in Earth's mantle, using a range of numbers explained in Appendix A and tabulated in Table 1. Equilibration lengths range from <1 mm to 10 m, and we use $\beta = 2 \times 10^{-6}$ m^{-1}; $c_h h/L_{eq}$ ranges from $O(1)$ to $O(10^6)$ when the compaction length is taken as 1000 m and from $O(10^{-2})$ to $O(10^4)$ when a compaction length is taken as 100 m. Parameter values that are believed to be characteristic of Earth's mantle are thus mostly in the regime that allows for rapid growth of stationary channels.

The effect of diffusion (Appendix B) is also investigated. When diffusion is strong enough, it will cause an increase in channel spacing and a decrease in channel growth rate. However, this will not inhibit the channels from growing.

The forming channels are elongated and span the vertical box size. Their amplitude increases with height, thus showing increasing chemical disequilibration as liquid ascends in the melting column. When Da is high, chemical disequilibration is small, but dissolution of channel is most efficient. Hence soluble phases may become reduced in volume or completely exhausted. When channels thus become stripped of soluble phases (i.e., stripped of pyroxene but not of olivine), melt flowing through them will be effectively isolated from equilibration with these phases. Since the channels span the system vertically, they can bring to the surface melt that has not equilibrated with its surroundings since it began its ascent at the bottom of the melting column. This may explain why MORB is out of chemical equilibrium with upper mantle peridotites [*Johnson et al.*, 1990] and includes chemical signatures from the bottom of the melting column [*Klein and Langmuir*, 1987; *Salters and Hart*, 1989].

Channels formed as a result of this instability should be identifiable in the geologic record. Their contact relationships should be indicative of replacement of host peridotite as a result of selective dissolution of more soluble phases (i.e., pyroxene). Additionally, minerals in dissolution channels should be close to equilibrium with MORB and therefore will have very different minor and trace element compositions from the same minerals in surrounding peridotite. In fact, these characteristics are observed in dunite bodies within the residual mantle peridotite section of the Oman ophiolite [*Kelemen et al.*, 1995b].

However, we emphasize that the results of the present study may not be directly applicable to the mantle. In particular, the morphology of dissolution channels arising from this instability, developing over finite length scales and timescales, cannot be predicted from linear stability analysis. Additionally, the multicomponent melt migration process in the earth with the inclusion of advective heat transport and background melting effects is more complicated than the problem studied here and is a topic for ongoing studies.

In addition to the formation of stationary dissolution channels, another coexisting linear solution indicates the existence of traveling compaction-dissolution waves, whose amplitude increases with time. These unstable waves, pockets of undersaturated melt in a high porosity region, will transport increasingly undersaturated melts to the surface even when the matrix is too weak to support stationary channels. They may also aid in explaining the production and growth of "magmons," compaction waves previously thought to be generated by an initial step in porosity.

Appendix A: Discussion of Parameter Values for the Mantle

Table 1 illustrates the derivation of a range of Damköhler numbers which may be applicable to porous flow of melt in the mantle. The results are tabulated in two ways, in terms of an "equilibration length," and in terms of Damköhler number for a fixed system length scale of 100 m. In our study, the equilibration length, $L_{eq} = \phi\rho_f w_0/R_{eff}$, is the length over which fluid will advect before equilibrating with its surroundings.

Critical input parameters in determining equilibration lengths for the mantle are the crystal dissolution rate and the melt flow velocity. We present a broad range of possible values, because the estimation of effective dissolution rates, porosity and fluid velocity are so uncertain. Several studies have measured dissolution of mantle minerals in basaltic melts at upper mantle pressures and temperatures [*Kuo and Kirkpatrick*, 1985; *Brearley et al.*, 1986; *Zhang et al.*, 1989]. All of these indicate that measured dissolution rates are diffusion controlled, and thus depend on the diffusivity of the dissolving species and the width of a chemical boundary layer around the dissolving crystal. The first two studies emphasized results for relatively "well-stirred" melts, with narrow chemical boundary layers, while Zhang et al. attempted to minimize convection and mixing in liquids surrounding dissolving crystals, maximizing the

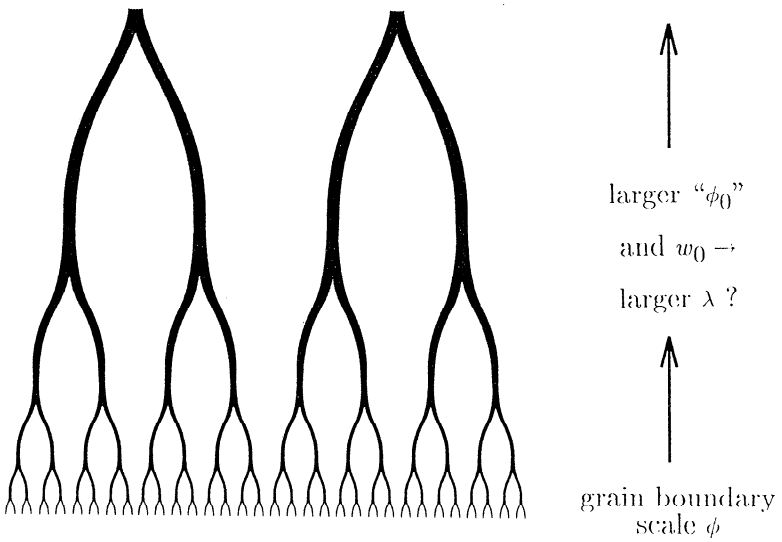

Figure A1. When high-porosity channels form, the solid-liquid surface area per unit volume is reduced and the characteristic equilibration length of the system will increase. This means that the wavelength of the channels will increase as well (from equation (55)). If we also consider the increase in melt velocity with height, we get an additional increase in L_{eq}. Thus we can tentatively propose the following picture: narrow channels that form deep in the melting column will act as the background porous structure for a higher level and, due to the increase in horizontal wavelength with equilibration length, will coalesce to form an interconnected network of high porosity tubes similar to the upside down "fractal tree" proposed by *Hart* [1993].

width of the chemical boundary layer. It is difficult to know which of these apply to the microscopic geometry of melt flow in the mantle, below the continuum or Darcy scale, in which some intergranular pores could be effectively stagnant, while others may carry rapidly moving liquids. For this reason, we use linear dissolution rates derived from these studies ranging from 10^{-8} to 10^{-12} m/s. We convert volume to weight units using an approximate density of 3000 kg m^{-3} to obtain the reaction rate constant, R.

To obtain effective dissolution rates (kg s^{-1} m^{-3}), we calculated effective surface areas over which dissolution could occur in mantle peridotites, per unit volume. This calculation requires estimation of the grain size, grain shape, proportion of solid/liquid surface area to total surface area, and proportion of soluble phases in the peridotite. Pyroxene is much more soluble than olivine in ascending liquids [e.g., *Kelemen*, 1990; *Kelemen et al.*, 1995a], so for the purposes of this calculation we assumed that the proportion of soluble phases was the proportion of pyroxene in mantle peridotite. We have used the work of *VonBargen and Waff* [1986] to estimate solid-liquid surface areas for basalt-mantle systems as a function of porosity. In calculating the solid surface area per unit volume, we have assumed cube-shaped grains with linear dimensions from 0.01 to 0.5 cm.

Kelemen et al. [1995a] calculated peridotite solubilities in typical melts along likely adiabatic P-T gradients beneath mido-ocean ridges, using a thermodynamic model for partially molten silicate systems. Thus this calculation incorporates the effect of the heat of fusion in limiting solid solubility. Results of these calculations were used to estimate an approximate value for the solubility gradient, given in Table 1. This calculation did not include the possible effects of advective heat transport by rising melt in high permeability channels. Potentially, if melt flux becomes large enough, this could result in local heating of channels to temperatures higher than the adiabat for partially melting mantle peridotite. If this occurred, it would increase the local solubility of solid phases to values higher than those in Table 1, and act to further enhance growth of channels.

Steady state melt flow velocities were calculated using the reasoning of *Spiegelman* [1993c], in which the Darcy flux, $\phi w_0 = FV_0$ (where F is integrated mass fraction of melting and V_0 is solid upwelling rate) for ascending mantle beneath a spreading ridge. Another simplification can be made if ϕ is constant [e.g., *Johnson and Dick*, 1992; *Sobolev and Shimizu*, 1993]. In this formulation, if ϕ is much smaller than F, flow velocities are much greater than if the porosity is of the same order as the melt fraction. A range of values is used in Table 1 to investigate the maximum and minimum equilibration lengths likely in the mantle. Equilibration lengths calculated in this way range from Angstroms to meters.

The attempt to quantify effective reactive surface area brings about an interesting hypothesis about the finite size behavior of these channels: When high porosity channels form, the solid-liquid surface area per unit volume is reduced and the characteristic equilibration length of the system will increase. Hence the horizontal wavelength of the channels will grow (from equation (55)). Increasing melt velocity with height results in an additional increase in L_{eq}. A tentative sketch of finite size behavior is given in Figure A1.

Appendix B: Finite Diffusion

Diffusion in a porous medium is a result of hydrodynamic dispersion and molecular diffusion. Dispersion, in most cases, is associated with larger diffusion coefficients than molecular diffusion. Both have the effect of of causing an initial sharp concentration gradient to spread out with time. This appendix addresses the question of whether a finite diffusion rate will smooth out gradients in the concentration field to a point where the channeling instability will not be able to grow.

Predictions

It is probable that perturbations smaller than a diffusion length will be smoothed out. When diffusion is weak, and a diffusion length is smaller than the most unstable wavelength determined by reaction (as calculated for the no diffusion case above), diffusion will only act as a short-wave cutoff. When diffusion is strong, and a diffusion length is longer than the most unstable wavelength determined by reaction alone, it will allow for unstable growth but modify the dominant horizontal wavelength, forcing it to become longer than a diffusion length. This is because, as seen in Figure 3, all wavelengths are unstable in the presence of reaction alone (in the rigid case) and when short waves are damped, long wavelengths can become the fastest growing in the system. It follows that for strong diffusion, the growth rate will be lowered compared to the case with no diffusion.

Simplified Calculations

We present here a somewhat simplified linear analysis for the finite diffusion case. We allow for diffusion only in the horizontal direction, since allowing for vertical diffusion adds higher order derivatives in the vertical direction, complicating the vertical structure of the equations beyond the point necessary to obtain well-behaved solutions to the stability problem. This approximation is probably justified, since the vertical melt velocity is believed to be much larger than diffusion rates. However, one should note that available experimental diffusivities in silicate melts, quoted in Table 1, do not include effects of dispersion.

Solving the perturbation equations (36)-(40) with a finite value for $1/Pe$, (46) will have the form

$$m^3 + (Da + l^2/Pe - \frac{n}{\alpha\sigma})m^2 - (l^2 + \frac{nDa}{\alpha\sigma})m + l^2 Da\frac{n\rho_f}{\rho_s\sigma} - l^2(Da + l^2/Pe) = 0. \quad \text{(B1)}$$

The growth rate is again decomposed into compaction and reaction parts

$$\sigma = \sigma_C + \sigma_{Da} \quad \text{(B2)}$$

where the compaction contribution to the growth rate is

$$\sigma_C = \frac{1}{\alpha}\frac{nm}{(m^2 - l^2)} \quad \text{(B3)}$$

and now

$$\sigma_{Da} = -\frac{nl^2 Da\frac{\rho_f}{\rho_s}}{(m^2 - l^2)(m + Da + l^2/Pe)} \quad \text{(B4)}$$

is the diffusion-reaction contribution to the growth rate. In the limit of $l \to \infty$, $\sigma_{Da} \to 0$, as expected since diffusion will tend to damp the growth of short wavelength perturbations.

We use boundary conditions (47) to solve (B1) following the same numerical procedure outlined in the "unstable stationary channels" section. Figure B1 demonstrates the effect of adding diffusion to the no-diffusion solution obtained for the rigid medium. Generally, diffusion acts to reduce the growth rate of the instability and to shift the most unstable wavelength to become longer than in the no diffusion case, as predicted.

Figure B2 shows the most unstable wavelength and its growth rate for a constant $Da = 10$ and a varying Pe number. The qualitative behavior is as predicted: for weak diffusion ($Pe \gg Da$, which corresponds to the condition when equation (17) can be considered diffusionless) the most unstable wavelength and its growth rate remain nearly the same as the case with no diffusion. For $Pe \ll Da$ the dominant wavelength λ_x increases with increasing diffusion length (decreasing Pe) $\lambda_x \propto (1/Pe)^{1/4}$, and the growth rate is reduced but remains positive.

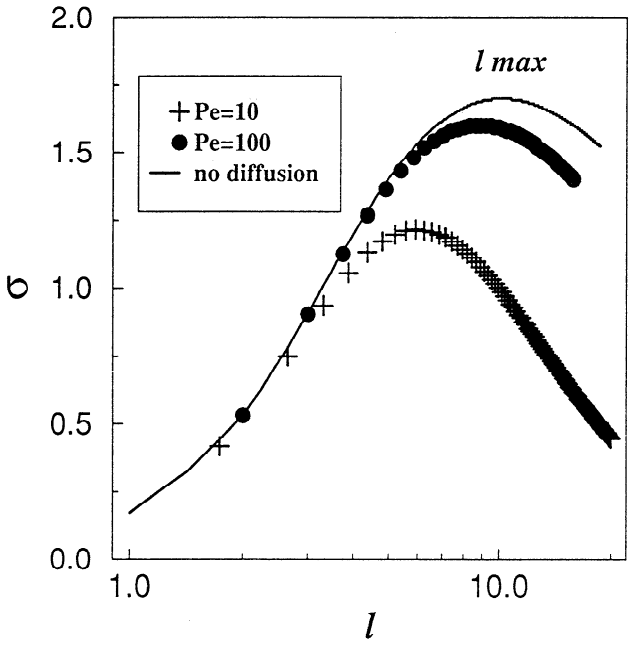

Figure B1. Growth rate σ as function of horizontal wavenumber l for a rigid matrix with $Da = 10$ for various diffusion coefficients. Solid line is the growth rate in the case of no diffusion, replotted from Figure 3. Solid circles are the linear stability analysis results for a rigid system with weak diffusion, $Pe = 100$. Strong diffusion with $Pe = 10$ is shown in crosses. The horizontal wavelength ($= 2\pi/l_{\max}$) of forming channels becomes larger in the presence of diffusion and the growth rate is somewhat lowered, but the nature and the robustness of the instability are not changed. These results are in agreement with scaling arguments in Appendix B.

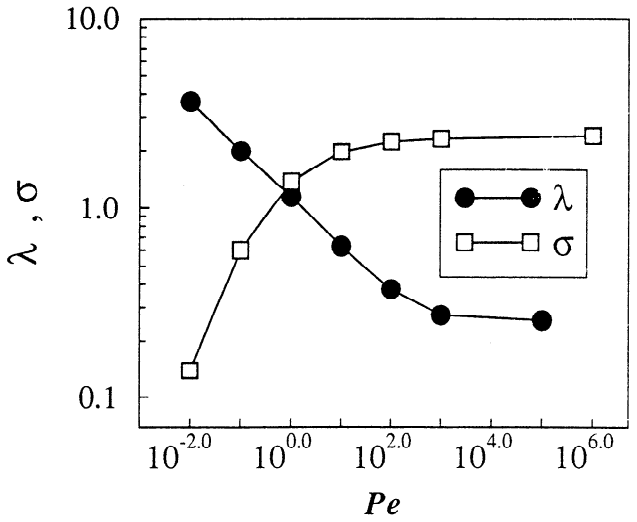

Figure B2. The fastest growing horizontal wavelength, $\lambda_x = 2\pi/l_{\max}$, derived from plots similar to Figure B1 with different Pe numbers, for a rigid medium with a constant $Da = 10$, plotted by solid circles. In the case of strong diffusion, when $Pe < Da$, $\lambda_x^4 \propto 1/Pe$. On the same plot we show the growth rate σ by open squares, to be unaffected by diffusion when Pe is large but to be reduced when diffusion becomes important. Channels will grow ($\sigma > 0$) for all diffusion rates.

Thus we conclude that when diffusion is strong or when the Pe number is of the same order of magnitude as the Da number, the addition of diffusion can alter channel spacing and lower the growth rate but cannot inhibit the instability from growing. When diffusion is weak ($Pe \gg Da$), it can be neglected altogether.

Acknowledgments. This work was supported by NSF Grant OCE-9314013. E.A. was also supported by the sponsors of the MIT Porous Flow Project. The authors would like to thank B. Evens, C. Helfrich, J. Olson, D. Rothman and A. Thompson for helpful and interesting discussions and suggestions.

References

Barcilon, V., and F. Richter, Nonlinear waves in compacting media, *J. Fluid Mech.*, *164*, 429–448, 1986.

Boudier, F., and A. Nicolas, Structural controls on partial melting in the Lanzo peridotites, in *Magma Genesis*, edited by H. B. Dick, pp. 63–78, Portland. Oreg. Dep. of Geol. and Miner. Ind., 1977.

Brearley, M., C. Scarfe, and H. Brenner, Dissolution rates of upper mantle minerals in an alkali basalt melt at high presssure: An experimental study and implications for ultramafic xenolith survival, *J. Petrol.*, *27*, 1157–1182, 1986.

Chadam, J., D. Hoff, E. Merino, P. Ortoleva, and A. Sen, Reactive infiltration instability, *IMA J. Appl. Math.*, *36*, 207–221, 1986.

Dick, H., Evidence of partial melting in the Josephine peridotite, in *Magma Genesis*, edited by H. B. Dick, pp. 63–78, Portland. Oreg. Dep. of Geol. and Miner. Ind., 1977.

Hart, S. R., Equilibration during mantle melting: A fractal tree model, *Proc. Natl. Acad. Sci. U.S.A.*, *90*, 11,914–11,918, 1993.

Hinch, G., and B. S. Bhatt, Stability of an acid front moving through porous rock, *J. Fluid Mech.*, *212*, 279–288, 1990.

Hoefner, M., and H. Fogler, Pore evolution and channel formation during flow and reaction in porous media, *AIChE J.*, *34*, 45–54, 1988.

Hofmann, A. W., Diffusion in natural silicate melt: A critical review, in *Physics of melt migration*, edited by R. B. Hargraves, pp. 385–417. Princton Univ. Press, Princton, N.J., 1980.

Iwamori, H., A model for disequilibrium mantle melting incorporating melt transport by porous and channel flows, *Nature*, *366*, 734–737, 1993.

Johnson, K., and H. Dick, Open system melting and the temporal and spatial variation of peridotite and basalt compositions at the Atlantis II fracture zone, *J. Geophys. Res.*, *97*, 9219–9241, 1992.

Johnson, K., H. Dick, and N. Shimizu, Melting in the oceanic upper mantle: An ion microprobe study, *J. Geophys. Res.*, *95*, 2661–2678, 1990.

Kelemen, P., Reaction between ultramafic wall rock and fractionating basaltic magma, *J. Petrol.*, *31*, 51–98, 1990.

Kelemen, P., and H. Dick, Focused melt flow and localised deformation in the upper mantle: Juxtaposition of replacive dunite and ductile shear zones in the Josephine peridotite, SW Oregon, *J. Geophys. Res.*, *100*, 423–438, 1995.

Kelemen, P., H. Dick, and J. Quick, Production of harzburgite by pervasive melt rock-reaction in the upper mantle, *Nature*, *358*, 635–641, 1992.

Kelemen, P., N. Shimizu, and V. Salters, Focused flow of melt in the upper mantle: Extraction of MORB beneath oceanic spreading ridges, *Mineral Mag.*, *58A*, 466–467, 1994.

Kelemen, P., J. Whitehead, E. Aharonov, and K. Jordahl, Experiments on flow focusing in soluble porous media with applications to melt extraction from the mantle, *J. Geophys. Res.*, *100*, 475–496, 1995a.

Kelemen, P. B., N. Shimizu, and V. J. Salters, Extraction of MORB from the upwelling mantle by focused flow of melt in dunite channels, *Nature*, *375*, 747–753, 1995b.

Klein, E. M., and C. H. Langmuir, Global correlations of oceanic ridge basalt chemistry with axial depth and crustal thickness, *J. Geophys. Res.*, *92*, 8089–8115, 1987.

Kuo, L. C., and R. J. Kirkpatrick, Kinetics of crystal dissolution in the system diopside-forsterite-silica, *Am. J. Sci.*, *285*, 51–90, 1985.

McKenzie, D., The generation and compaction of partially molten rock, *J. Petrol.*, *25*, 713–765, 1984.

Nicolas, A., *Structures of Ophiolites and Dynamics of Oceanic Lithosphere*. Kluwer Academic, Norwell, Mass., 1989.

Nicolas, A., Melt extraction from mantle peridotites: Hydrofracturing and porous flow, with consequences for oceanic ridge activity., in *Magma Transport and Storage*, edited by M. Ryan, pp. 159–174. John Wiley, New York, 1990.

Ortoleva, P., E. Merino, C. Moore, and J. Chadam, Geochemical self-organization, I, reaction-transport feedbacks, *Am. J. Sci.*, *287*, 979–1007, 1987.

Quick, J., The origin and significance of large, tabular dunite bodies in the Trinity peridotite, northern California, *Contrib. Mineral. Petrol.*, *78*, 413–422, 1981.

Salters, V. J. M., and S. Hart, The Hf-paradox and the role of garnet in the MORB source, *Nature*, *342*, 420–422, 1989.

Scott, D., The competition between percolation and circulation in a deformable porous medium, *J. Geophys. Res.*, *93*, 6451–6462, 1988.

Scott, D., and D. Stevenson, Magma ascent by porous flow, *J. Geophys. Res.*, *91*, 9283–9293, 1986.

Sleep, N., Formation of oceanic crust: Some thermal constraints, *J. Geophys. Res.*, *80*, 4037–4042, 1975.

Sleep, N., Tapping of melt by veins and dykes, *J. Geophys. Res.*, *93*, 10255–10272, 1988.

Sobolev, A. V., and N. Shimizu, Ultra-depleted primary melt included in an olivine from the Mid-Atlantic Ridge, *Nature*, *363*, 151–154, 1993.

Spiegelman, M., Flow in deformable porous media, 1, Simple analysis, *J. Fluid Mech.*, *247*, 39–63, 1993a.

Spiegelman, M., Flow in deformable porous media, 2, Numerical analysis — the relationship between shock waves and solitary waves., *J. Fluid Mech.*, *247*, 17–38, 1993b.

Spiegelman, M., Physics of melt extraction: Theory, implications and applications, *Philos. Trans. R. Soc. London A*, *342*, 23–41, 1993c.

Spiegelman, M., and P. Kenyon, The requirements for chemical disequilibrium during magma migration., *Earth. Planet. Sci. Lett.*, *109*, 611–620, 1992.

Steefel, C., and A. Lasaga, Evolution of dissolution patterns, in *Chemical Modeling in Aqueous Systems II*, edited by D. Melchior, and R. Bassett, pp. 212–225. Am. Chem. Soc., Washington, D.C., 1990.

Stevenson, D., Spontaneous small-scale melt segregation in partial melts undergoing deformation, *Geophys. Res. Lett..*, *16*, 1067-1070, 1989.

Turcotte, D., and G. Schubert, *Geodynamics, Application of Continuum Physics to Geological Problems*. John Wiley, New York, 1982.

VonBargen, N., and H. Waff, Permeabilities, interfacial areas and curvatures of partially molten systems: Results of numerical computations of equilibrium microstructures, *J. Geophys. Res.*, *91*, 9261–9276, 1986.

Zhang, Y., D. Walker, and C. Lesher, Diffusive crystal dissolution, *Contrib. Mineral. Petrol.*, *102*, 492–513, 1989.

E. Aharononv, Department of Earth, Atmospheric and Planetary Sciences, Room 54-616, Massachusetts Institute of Technology, Cambridge, MA 02139 (e-mail:einat@segovia.mit.edu)

P. B. Kelemen and J. A. Whitehead, Woods Hole Oceanographic Institution, Woods Hole, MA 02543 (e-mail: peterk@cliff.whoi.edu; jwhitehead@whoi.edu)

M. Spiegelman, Lamont-Doherty Earth Observatory of Columbia University, Palisades, NY 10964 (e-mail: mspieg@ldeo.columbia.edu)

(Received December 5, 1994; revised April 18, 1995; accepted April 24, 1995.)